Eleventh International Conference on Computational Fluid Dynamics (ICCFD11), Maui, Hawaii, USA, July 11-15, 2022

ICCFD11-2022-1401

Conservative Overset for Discontinuous Galerkin Methods

S. Tran* and J. Sitaraman**
* Science & Technology Corporation, USA.
** U.S. Army Combat Capabilities Development Command, Aviation & Missile Center, USA.

June 24, 2022

Abstract: This work is focused on developing an overset algorithm for the Discontinuous Galerkin Finite Element Method (DGFEM) that is conservative as well as high order. This approach involves modifying the formulation so that the overlap region between the overset grids is "cut" from the fringe elements. The cutting process is done purely in the formulation and no remeshing is required. This methodology is developed for both 1D and 2D DGFEM and tested for 1D linear advection, 1D inviscid Burger's equation, and 2D Euler equations. For all cases, the conservative overset method significantly reduced the overset conservation error to be on par with that of a single continuous mesh. On the other hand, traditional overset methods using pure interpolation produced errors approximately 5-6 orders of magnitude higher. Furthermore, for 1D linear advection the convergence rate was slightly improved by using conservative overset. The main drawback of this method is its lack of numerical stability, though this can be improved to some extent through regularization and careful choice of the cutting location.

Keywords: Overset Methods, Discontinuous Galerkin, Finite Element Methods

1 Introduction

Overset methods are a branch of computational fluid dynamics (CFD) which solve the governing equations over a computational domain comprised of several overlapping meshes. This class of methods is powerful because it allows for the study of cases involving large scale, unsteady motions as well as utilizing multiple solvers and numerical schemes within a single CFD simulation. Throughout these overset simulations, the solution at the boundaries of these meshes, also known as the fringe elements, needs to be communicated to neighboring meshes through interpolation. The interpolation schemes that most overset solvers routinely use are typically limited to second-order accuracy. Furthermore, they are non-conservative and non-convex when interpolating cell-centered data. Generally overset conservation error is not considered to be significant but as the CFD community moves towards utilizing high order solvers, developing conservative high order interpolation methods will be needed to maintain the order of accuracy throughout the simulation.

Several approaches to fully conservative overset methods have been reported in the literature in the past. In general two themes are explored: (1) trim away the overlap and re-grid the cavity between the two mesh systems [1, 2, 3, 4] and (2) cut one of the grids with the other and conservatively interpolate the solution field onto overlapping cells [5]. In general, these approaches have been used for static overlapping meshes and are reported to incur high computational overhead. More recently, Chandar [6] developed a finite volume method which removed the effect of the overlap region by implementing a flux correction both iteratively and implicitly. Kopriva et al. [7] have formulated a two-way coupling scheme that uses penalty functions to satisfy conservation and entropy stability for the special case of linear PDEs. Numerical verification of this method has not been performed yet however.

Another approach developed for the Discontinuous Galerkin Finite Element Method (DGFEM) by Galbraith [8] and extended by Crabill [9] and Duan [10] follows the abutting grid approach where a minimal overlap is created and the fluxes at the open faces of the abutting cells are exchanged between the mesh

systems. Note that this approach is not fully conservative because of the double counting of the overlapped regions, i.e the region enclosed by the set of abutting faces. However, careful optimization of the abutting face locations and solution interpolation can yield a conservation error that is of the order of discretization error. Building upon previous work on the abutting grid approach, this work aims to develop an overset method for the DGFEM which is conservative, amenable to high order methods, and requires no regridding.

2 Methodology

2.1 Discontinuous Galerkin Finite Element Formulation

Consider the generic advection equation shown below.

$$q_{,t} + F_{,x} = 0 \tag{1}$$

where x denotes space, t is time, q is the primary variable of interest, and F is some flux function that may be a function of x and t. Note that Einstein notation is used throughout this paper.

Following the traditional finite element formulation, Equation (1) is multiplied by an arbitrary weighting function, w, and then is integrated over the domain. Using integration by parts, we arrive at (2).

$$\int_{\Omega} \left[w q_{,t} - w_{,x} F \right] d\Omega + \int_{\Gamma} \left[w F \cdot \mathbf{n} \right] d\Gamma = 0 \tag{2}$$

where $\mathbf{n}$ is the normal vector, Ω represents the domain, and Γ represents the boundaries of the domain. Next, the domain is split up into a number of discrete elements, described by Equation (3).

$$\int_{\Omega_e} \left[w q_{,t} - w_{,x} F \right] d\Omega_e + \int_{\Gamma_e} \left[w F \cdot \mathbf{n} \right] d\Gamma_e = 0 \tag{3}$$

Quantities with the subscript e denote elemental quantities. Next the weighting function and unknown variables are decomposed into the products of spatially-varying shape functions and time-varying coefficients as follows:

$$w(x,t) = \sum_{a=1}^{nshp} N_a(x) \widehat{w}_a(t) \tag{4}$$

$$q(x,t) = \sum_{a=1}^{nshp} N_a(x) \widehat{q}_a(t) \tag{5}$$

where $N(x)$ are the shape functions, $nshp$ is the total number of shape functions on any given element, and the superscript $\widehat{(\cdot)}$ denotes the time-varying coefficients. The weighting function and the unknown variable are assumed to occupy the same space so that the same shape functions can be used for both w and q. The exact shape functions, which are generally polynomials, can be chosen based on ease of implementation. Throughout this work, Legendre bases are used.

After substituting Equations (4) and (5) into Equation (3) and recognizing that the weighting functions are arbitrary and that their coefficients may be factored out, we arrive at the following equation:

$$\int_{\Omega_e} \left[N_a N_b \widehat{q}_{b,t} - N_{a,x} F(N_b, \widehat{q}_b) \right] d\Omega_e + \int_{\Gamma_e} \left[N_a F(N_b, \widehat{q}_b) \cdot \mathbf{n} \right] d\Gamma_e = 0 \tag{6}$$

Einstein notation is used so repeated indices imply a summation. Factoring out the time derivative of the weights, $\widehat{q}_{b,t}$, and rearranging the terms, the final semi-discrete form of the equation can be found.

$$\mathcal{M}(N_a, N_b) \widehat{q}_{b,t} = \mathcal{V}(N_a, N_b, \widehat{q}_b) - \mathcal{B}(N_a, N_b, \widehat{q}_b, \mathbf{n}) \tag{7}$$

where each of the terms is one of the integral terms defined by

$$\mathcal{M}(N_a, N_b) = \int_{\Omega_e} N_a N_b d\Omega_e \tag{8}$$

$$\mathcal{V}(N_a, N_b, \widehat{q}_b) = \int_{\Omega_e} N_{a,x} F(N_b, \widehat{q}_b) d\Omega_e \tag{9}$$

$$\mathcal{B}(N_a, N_b, \widehat{q}_b, \mathbf{n}) = \int_{\Gamma_e} \left[N_a F(N_b, \widehat{q}_b) \cdot \mathbf{n}\right] d\Gamma_e \tag{10}$$

Observe that this represents a system of equations where $\mathcal{M}(N_a, N_b)$, called the "mass matrix," is a matrix of size $nshp \times nshp$ whereas $\mathcal{V}(N_a, N_b, \widehat{q}_b)$ and $\mathcal{B}(N_a, N_b, \widehat{q}_b, \mathbf{n})$, the volume and boundary terms, respectively, are vectors of length $nshp$. Using the discontinuous Galerkin finite element (DGFEM) approach, this system of equations is formulated for each element separately rather than as a large global system. Note that each element is coupled to its neighboring elements only through the boundary terms.

In terms of the boundary fluxes, there is no requirement for the values of q to be continuous across elements using DGFEM, as shown in Figure 1. Thus, special care must be taken with the boundary integrals, in order to approximate the inter-element fluxes. There are a number of ways to do this but in this work, the fluxes are accounted for using the Lax-Friedrichs flux shown in Equation 11 for the 1D case.

$$q|_{\Gamma_e} \approx 0.5(q_L + q_R) - 0.5|c|(q_R - q_L)) \tag{11}$$

where q_L and q_R represent the interior and exterior states of q across the element boundaries and c is the convection speed.

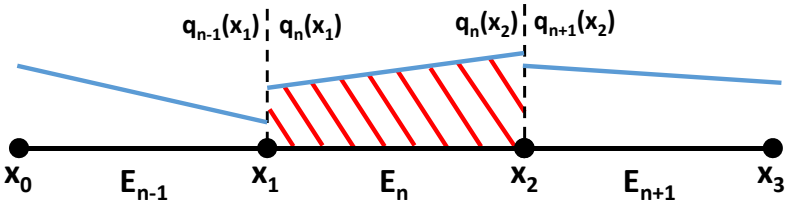

Figure 1: Schematic describing a conventional DGFEM scheme on a single mesh, with fluxes calculated at the discontinuous boundaries and volume integrals calculated over the element (shown in striped red)

Gauss-Legendre quadrature is used in order to compute the volume integrals needed for $\mathcal{M}(N_a, N_b)$ and $\mathcal{V}(N_a, N_b, \widehat{q}_b)$. Time integration was done using the explicit third order Runge Kutta scheme.

2.2 1D Baseline Overset Method

Consider two 1D grids, called M1 and M2, where M2 is finer than M1 and is completely overlapping M1. In order to conduct the oversetting, the solver must first generate a minimum overlap between the two grids. Cells in both grids are blanked until the two grids only overlap at a single element at the boundaries of both meshes, as shown in Figure 2. This will be referred to as a "minimum overlap." These minimally overlapping fringe elements are where information is passed between the two grids.

In DGFEM, information enters and exits an element solely through the boundary flux terms so these terms must be modified in the fringe elements to allow for passing of information from the overlapping grid. The first method of doing so will be referred to as the baseline overset method and is explained visually in Figure 2. In this figure, the two overlapping fringe elements are $E_{M1,n}$ on mesh M1 and element $E_{M2,1}$ on mesh M2.

In order to compute the boundary integrals in Equations (10), the interior and exterior states of the variables must be found. For the non-fringe elements, the exterior states are found at the coincident boundary points of the adjacent elements. For fringe elements, one of the boundary nodes is not connected to any other elements in the mesh and instead is overlapping with an element on the neighboring mesh due to the minimum overlap (see the nodes at x_0 and $x_{1/2}$ in Figure 2). Computing the exterior states at these fringe

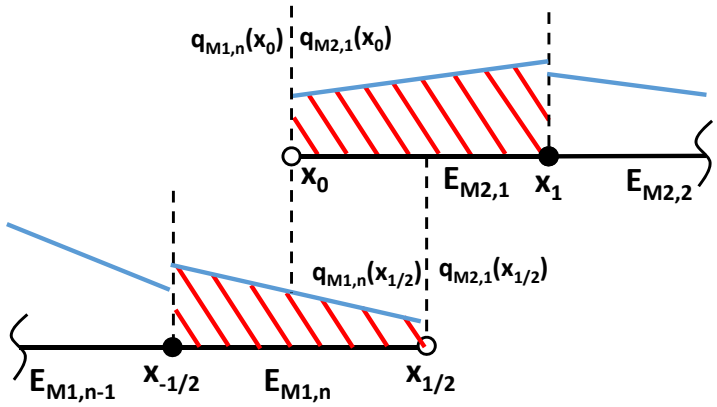

Figure 2: Schematic describing the baseline overset DG method with two meshes. Fluxes from neighboring meshes are interpolated at the element endpoints and volume integrals are calculated over the complete elements (shown in striped red)

boundary nodes is straightforward and just requires each fringe element to interpolate the states at these interior points using Equation (5) and then communicate them to their counterpart on the opposite mesh. This exchange is completed every time the residual vector is computed.

Using the baseline overset method, the volume integrals for the mass matrix and the contribution to the residual vector by the convective terms are handled identically for both interior and fringe elements. This leads to an overlap region ($x = [x_0, x_{1/2}]$ in Figure 2) that is integrated over twice, once by each fringe element, during the timestep. This is one source of conservation error in the simulation [6]. The boundary fluxes of the fringe elements are also not evaluated at the exact same physical location, i.e. nodes x_0 and $x_{1/2}$ are not coincident. This is another source of conservation error since the fluxes transferred between the meshes will not cancel each other exactly.

2.3 1D Conservative Overset Method

The conservative overset approach is described visually in Figure 3 and its main goal is to remove the double counting of the overlap region discussed above. This is done through "cutting" the fringe elements so that each one only integrates over a subset of the overlap region. By doing so, the overset grids become conceptually similar to a single, fully connected grid. Note that this cutting procedure is purely conceptual and is all carried out through modifications to the equations. No remeshing is needed.

First, the overlap region $[x_0, x_{1/2}]$ is divided between the two fringe elements at some cut location, called x_{cut} in Figure 3. The location of x_{cut}, and therefore the proportion of how much each fringe cell is cut, is a controllable parameter. For instance, both meshes can have half of the overlap region removed from each of them or alternatively all of the overlapping region may be removed from just one of the fringe elements while the other is left untouched. While any combination of cutting is valid, there are implications for numerical stability that will be discussed in more detail below. As a rule, it is better to choose the cut location such that the proportion of each element being cut is minimized.

Once x_{cut} has been defined, both the volume and boundary terms are modified to effectively shorten the fringe elements. The volume integrals are adjusted to only account for the non-overlapping portion of the element. For the example shown in Figure 3, the volume integrals would only be computed for $E_{M1,n}$ between $x_{-1/2}$ and x_{cut} while the volume integrals for element $E_{M2,1}$ would span from x_{cut} to x_1. While this can be done through direct integration of the remaining element, doing it as an additional cutting step is simpler for more complex grids. For this reason, this approach will be the focus of this work and is described in Equation 12.

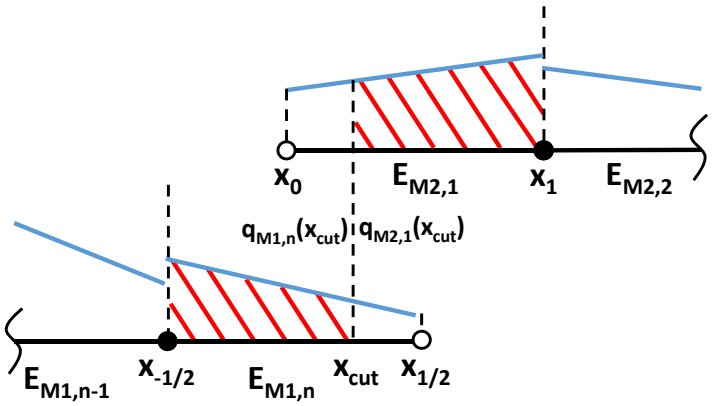

Figure 3: Schematic describing the conservative overset DG method with two meshes. Portions of the overlap region are removed from each of the volume integrals and the fluxes are calculated at the point where the overlap is split.

$$\begin{aligned}[\mathcal{M}(N_a,N_b)-\mathcal{M}_{cut}(N_a,N_b)]\,\widehat{q}_{b,t} = &[\mathcal{V}(N_a,N_b,\widehat{q}_b)-\mathcal{V}_{cut}(N_a,N_b,\widehat{q}_b)]\\ &-[\mathcal{B}(N_a,N_b,\widehat{q}_b,\mathbf{n})-\mathcal{B}_{cut}(N_a,N_b,\widehat{q}_b,\mathbf{n})]\end{aligned} \tag{12}$$

where the subscript *cut* indicates integrals over just the cut portion of the elements. In the example shown in Figure 3, this would correspond the region from x_{cut} to $x_{1/2}$ for element $E_{M1,n}$.

Note that the shape functions corresponding to the original uncut element (N_a and N_b) are used in the computing the cut integral terms, i.e. the cut regions are not treated as entirely new elements with their own bases. This is done for both ease of implementation as well as to be consistent with the DGFEM formulation of the equations. Furthermore, in this implementation the same number of quadrature points are used to compute both the integrals over the entire element and the integrals over the cut portion, thereby maintaining the order of accuracy for the integration. The cutting of the boundary integral terms is identical to simply interpolating the neighboring fluxes at the cut boundary location instead of the element endpoint in 1D.

There are several undesirable consequences of the cutting procedure on the mass matrix. The first is that by only integrating over a portion of the element, the orthogonality of the Legendre-based mass matrix is broken. When integrating over a partial element, the mass matrix is fully populated instead of being purely diagonal, as is the case normally for 1D.

The numerical stability of the scheme is also an issue. The larger the proportion of the element is removed, the more ill conditioned the mass matrix $\mathcal{M}-\mathcal{M}_{cut}$ becomes. This can ultimately lead to divergent solutions. This is demonstrated in Figure 4 which shows the condition number of the analytical mass matrix as a function of the amount of the element is cut. The condition number increases exponentially as more and more of the element is removed and the effect worsens for higher orders of accuracy. This behavior was observed for both Lagrange and Legendre bases.

For this reason, L2 (or Tikhonov) regularization is used to maintain stability during the mass matrix inversion. The regularization essentially solves a similar L2 minimization problem rather than directly inverting the mass matrix. While this is a more stable approach, it comes at the cost of additional bias (and conservation error). This is shown in Equation (13) for the generic problem $Ax = b$.

$$\left[A^TA+\Gamma^T\Gamma\right]x = A^Tb \tag{13}$$

where A is a matrix, b is the forcing vector, x is the solution, $\Gamma = \lambda I$ is the Tikhonov matrix, and λ is a tunable parameter which controls the amount of regularization added. The least amount of regularization is added in this work ($\lambda = 0$) in order to minimize the additional error. Furthermore, this additional step is applied only to the elements that are cut by more than 50% in order to reduce amount of additional bias

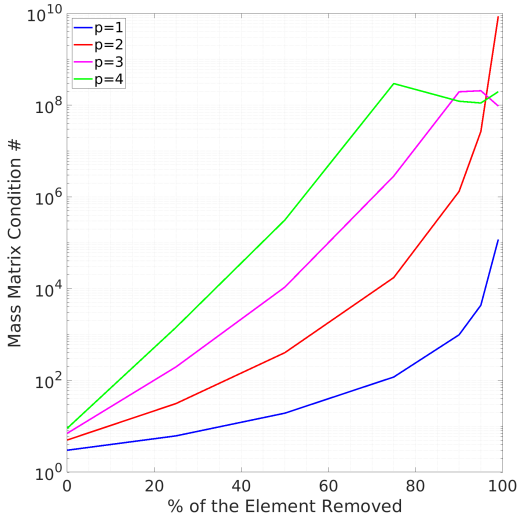

Figure 4: Condition number of the final mass matrix ($\mathcal{M} - \mathcal{M}_{cut}$) as a function of the percent of the element removed

added to the system. However even with this additional stability, the method fails if more than approximately 90% of the element is removed. Additional regularization may be added to further stabilize the method at higher orders however this was not pursued since adding too much bias may negate the benefits of using the conservative overset method. As stated before, the best way to maintain stability is to choose the cut location such that the proportion of each element being cut is minimized as much as possible.

2.4 2D Conservative Overset Method

When extending the conservative overset method to 2D, the overall goal of cutting fringe elements in order to prevent double integration in the mesh overlap region remains the same. Cutting 2D elements involves cutting both grids along some given "cut boundary" which is now a parametric curve. Finding a suitable cut boundary may be a challenge in the general case, especially for anisotropic unstructured grids. In this work, the simplest case where the cut boundary is a straight line is examined. Consider the two overlapping meshes shown in Figure 5a. Both grids are cut along a common cut boundary, indicated by the dashed line. Cutting each grid then becomes a process of cutting all of the individual triangles intersected by the cut boundary.

Now consider a single unstructured triangle that needs to be cut, as shown in Figure 5b. As shown in Equation (12), the element volume and boundary integrals over the original triangle can first be computed as normal and then are modified afterwards to account for the cut region. So the first step is to compute the terms over the entire element as normal. Based on the original DGFEM (Eq. (7)), the volume and boundary integrals may be computed using a number of quadrature points seeded across the element area and edges, respectively, as shown in Figure 6. In 2D the discontinuous fluxes across inter-element boundary edges are resolved using an upwind-biased flux-difference-splitting approach [11].

Next the cutting procedure begins which involves computing $\mathcal{M}_{cut}$, $\mathcal{V}_{cut}$, and $\mathcal{B}_{cut}$ and then subtracting them from the original terms $\mathcal{M}$, $\mathcal{V}$, and $\mathcal{B}$. In order to compute these cut terms, appropriate quadrature points need to be seeded throughout the cut region as shown in Figure 7. As before, the same number of quadrature points used for the full element are used in the cut element in order to maintain the order of integration. In order to find the location of these new quadrature points, the Jacobian of the cut cell must be found.

As with any classical finite element method, each physical triangle is mapped back to a given reference element through the use of a Jacobian matrix, J. For a straight sided triangle, the Jacobian is constant throughout the element and can be found based on the physical coordinates of the vertices. This allows for

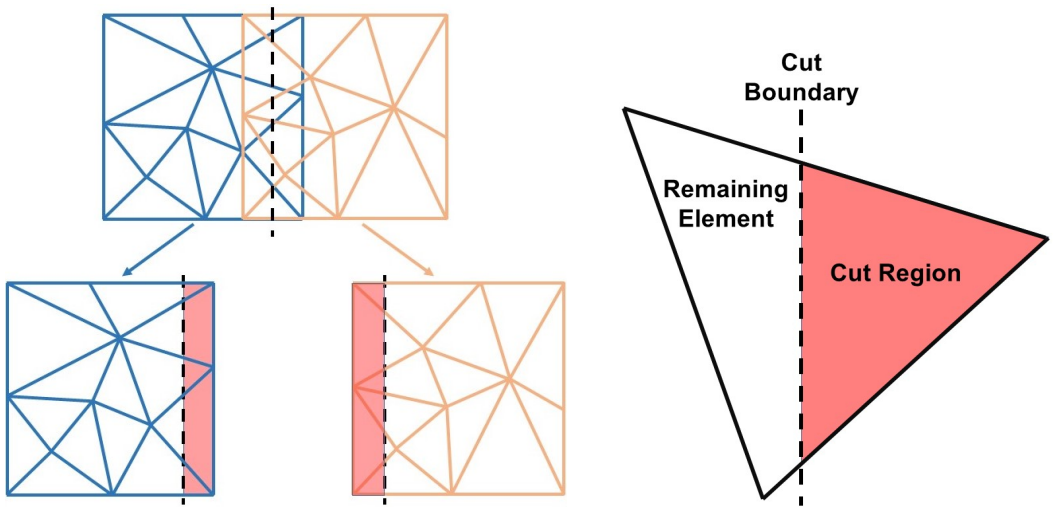

(a) Cut meshes (b) Cut triangle

Figure 5: Diagram showing the cutting of (a) two overset triangular meshes and (b) a single unstructured triangle

simple integration over unstructured triangles. The coordinate system in physical space will be denoted as (x, y) and the Barycentric coordinate system of the reference triangle is denoted as (r, s), as shown in Figure 8.

Since the location of the cut boundary is known, the coordinates of the cut region can be found analytically and a cut element Jacobian matrix J_{cut} may be computed. Using the Jacobians for both the original and cut cell, the coordinates of the cut cell quadrature points may be found relative to the original element's local Barycentric coordinate system. This is shown in Equation (14).

$$\begin{aligned}
\begin{bmatrix} r \\ s \end{bmatrix}_{full} &= J_{full}^{-1} \left(\begin{bmatrix} x \\ y \end{bmatrix}_{cut} - \begin{bmatrix} x_0 \\ y_0 \end{bmatrix}_{full} \right) \\
&= J_{full}^{-1} \left(\left(J_{cut} \begin{bmatrix} \partial r \\ \partial s \end{bmatrix}_{cut} + \begin{bmatrix} x_0 \\ y_0 \end{bmatrix}_{cut} \right) - \begin{bmatrix} x_0 \\ y_0 \end{bmatrix}_{full} \right) \\
&= \begin{bmatrix} \frac{\partial r}{\partial x} & \frac{\partial r}{\partial y} \\ \frac{\partial s}{\partial x} & \frac{\partial s}{\partial y} \end{bmatrix}_{full} \left(\left(\begin{bmatrix} \frac{\partial x}{\partial r} & \frac{\partial x}{\partial s} \\ \frac{\partial y}{\partial r} & \frac{\partial y}{\partial s} \end{bmatrix}_{cut} \begin{bmatrix} \partial r \\ \partial s \end{bmatrix}_{cut} + \begin{bmatrix} x_0 \\ y_0 \end{bmatrix}_{cut} \right) - \begin{bmatrix} x_0 \\ y_0 \end{bmatrix}_{full} \right)
\end{aligned} \tag{14}$$

where J_{full} is the Jacobian of the original uncut element, J_{cut} is the cut region Jacobian, (x_0, y_0) are the physical coordinates of the node which corresponds to $(r, s) = (0, 0)$ for either the original or cut triangle, and $(\partial r, \partial s)$ are the Barycentric coordinates of the quadrature points. All of these quantities are known because they are either prescribed (as is the case for $(\partial r, \partial s)$) or can be computed. Once $[r, s]_{full}$ is found for the cut region quadrature points, they can then be used to find the shape function values and derivatives, N_a and $N_{a,x}$. Afterwards it is straightforward to compute $\mathcal{M}_{cut}$ and $\mathcal{V}_{cut}$ in a similar manner as what was done for the original triangle.

Modifying the boundary integrals is more complicated as each face must be handled individually. Consider Figure 7b which shows the various edges involved in the cutting procedure. First, edge I-II is not cut so it is left untouched by the cutting procedure. Edges II-III and III-I intersect the cut boundary and thus the integral over the cut portion must be subtracted from the total boundary integral. Appropriate quadrature points are placed along the cut portion (i.e., edges V-III and III-IV) using Equation (14) and the fluxes over these cut edges are then integrated into B_{cut}. Note that the fluxes at these locations must be computed from both the local and neighboring elements in order to compute the Riemann flux at each of the cut cell quadrature points.

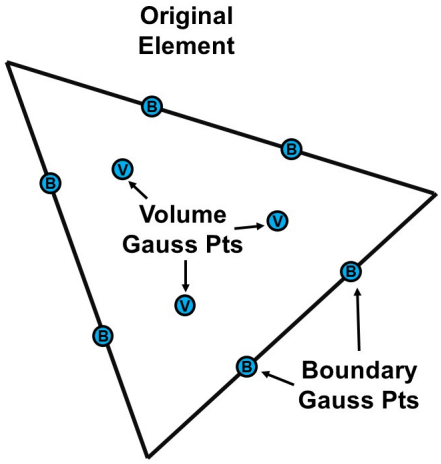

Figure 6: Diagram showing the computation of the volume and boundary integrals using the traditional DGFEM on a triangle

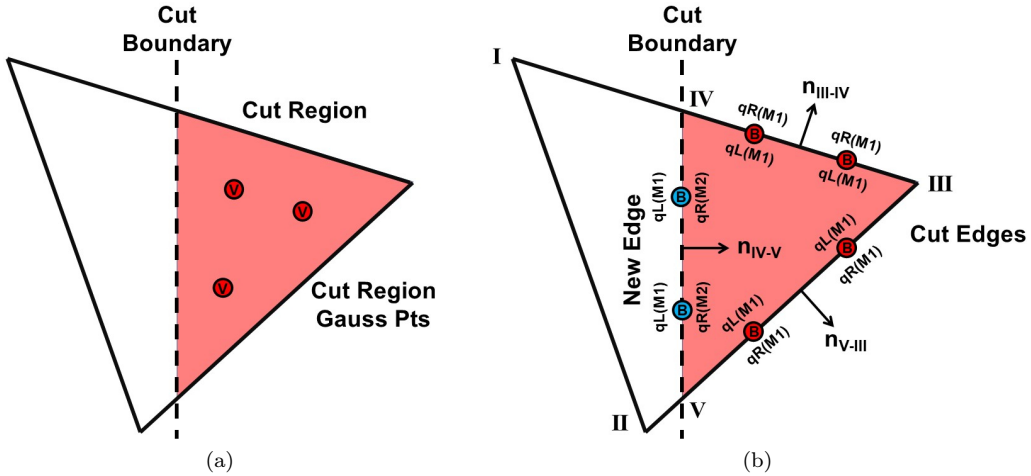

Figure 7: Diagram showing (a) the cut region seeded with quadrature points and (b) the cut edges seeded with quadrature points colored by whether the fluxes through that edge are removed (red) or added (blue)

Finally, additional fluxes coming into the element through the cut boundary must be accounted for. These fluxes correspond to the fluxes from the neighboring mesh. These fluxes enter the element through the new edge formed along line segment IV-V. Because these fluxes are being added to the system rather than being subtracted (as was done for edges III-IV and V-III), the sign and outward facing normal must be flipped as shown in Equation (15). For clarity, the normals, $\mathbf{n}$, for edge V-III and III-IV are pointing outwards and the normal for edge IV-V are pointing inwards as shown in Figure 7b.

$$\begin{aligned}\mathcal{B}_{cut} = &\int_{V-III} N_a N_b \widehat{q}_b \mathbf{n} d\Gamma + \int_{III-IV} N_a N_b \widehat{q}_b \mathbf{n} d\Gamma \\ &- \int_{IV-V} N_a N_b \widehat{q}_b \mathbf{n} d\Gamma\end{aligned} \tag{15}$$

The interior states (labeled q_L in Figure 7b) along the cut element edges are straightforward to compute since they are just interpolated using the current triangle's shape functions and weights. The exterior states (labeled q_R) along edges V-III and III-IV are interpolated from neighboring elements on the current mesh and are easily found. On the other hand, the q_R values along the cut boundary correspond to states associated

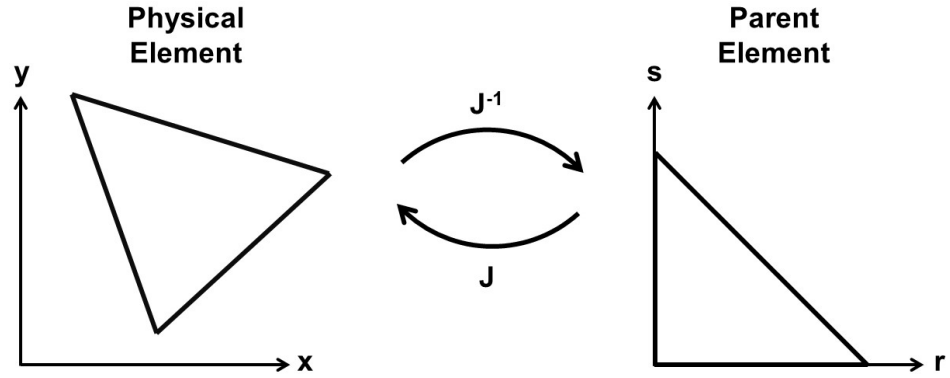

Figure 8: The mapping between the unstructured physical triangle and the reference element

with an element on the neighboring mesh. In order to find these exterior states, the physical coordinates of these quadrature points on each mesh are passed to the neighboring mesh. The meshes will then locate and interpolate the q values at these points before returning them to the original mesh.

Once these steps are done, it is possible to compute all of the cut element terms in Equation (12) and the cutting process can be completed for the element. This process is then repeated for every element intersected by the cut boundary on both of the grids.

As was the case in 1D, cutting the mass matrix may lead to numerical instabilities due to the mass matrix becoming ill conditioned. This is demonstrated in Figure 9. As the order of accuracy increases and as greater portions of the element are cut, the condition number of the mass matrix increases dramatically. This effect can be mitigated through finding cut boundaries which minimize the proportion of each fringe element being cut, however this is a nontrivial problem. Methods for finding these cut boundaries will be explored in greater detail in future works.

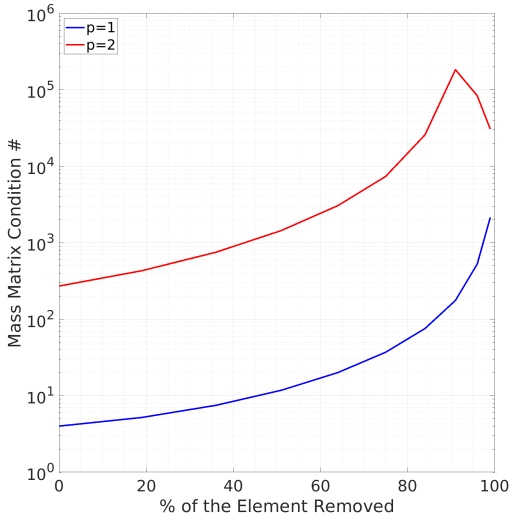

Figure 9: Condition number of the final mass matrix ($\mathcal{M} - \mathcal{M}_{cut}$) as a function of the percent of the element removed for 2D triangles

3 Applications

3.1 1D Linear Advection

The first problem of interest is the 1D advection equation, shown in its continuous strong form in Equation 16.

$$u_{,t} + cu_{,x} = 0 \tag{16}$$

u is the quantity of interest, c is the constant convection speed, and the other quantities are unchanged from their previous definition. The chosen initial condition is a Gaussian hill as shown in Equation (17) and Figure 10.

$$u(x,0) = 0.1\text{exp}(-20x^2) \tag{17}$$

Two overlapping grids are used for this case with the finer grid spanning [-0.50703125, 0.24296875] and chosen to be finer by a factor of 2. Periodic boundary conditions are imposed at the boundaries of the background mesh so as the hill advects in time, it will eventually return to its initial position at x=0. Due to the lack of dissipation in the governing equation, the exact solution is identical to the initial condition after the hill flows through the domain once. However due to numerical dissipation and discretization errors, the computed solution will have quantifiable differences. The L2 error and conservation errors can thereby be computed following Equations (18) and (19).

$$error_{L2} = ||u(x,T) - u(x,0)||_2 \tag{18}$$

$$error_{cons} = \left| \sum_{i=1}^{n_{elem}} \int_{\Omega_{e_i}} q(x,T) d\Omega_{e_i} - \sum_{i=1}^{n_{elem}} \int_{\Omega_{e_i}} q(x,0) d\Omega_{e_i} \right| \tag{19}$$

where T is the final time after a single flow-through, $||\cdot||_2$ indicates the L^2 norm, and $|\cdot|$ is the absolute value. Note that the integrals in these equations are computed only over the regions where the equations are being solved. In other words, for the baseline overset method, the overlap region will be integrated over twice and only once for the conservative method. This is consistent with how the governing equations were solved.

A convergence study is computed for this case at various orders of accuracy ranging from p = 1 to 4 using both the baseline and conservative overset methods. For both sets of cases, the timestep size was chosen such that the CFL = 0.05 based on the finest grid size to minimize temporal errors. For these cases, the entire overlap region was subtracted from the coarser fringe cell while the finer fringe cell was unmodified.

Both the L2 and conservation error are shown in Figure 11. For the L2 error, all of the cases followed the expected convergence rate. As expected, increasing the order of accuracy noticeably reduces the L2 error. Overall the conservative overset shows slightly better convergence than the baseline overset cases across the board. In terms of the conservation error, there is a clear difference between the performance of the two overset methods. The baseline overset method shows noticeable conservation error in the range of $O(10^{-3})$ to $O(10^{-11})$. On the other hand, the conservative overset method generally shows errors about 6 orders of magnitude lower than the baseline overset and the errors approach machine zero for finer grids for all orders.

As mentioned before, there are multiple valid approaches to dividing up the overlap region between the two grids. One could remove the full overlap region from just one of the fringe elements or remove a portion from each fringe element. The effect of this is studied for the case of p=1 and the results are shown in Tables 1 and 2. Overall the L2 and conservation errors remain relatively constant regardless of how much of the overlap was removed from each element. When the order of accuracy was increased to $p > 1$, a number of cases were unstable when the entire overlap region was removed from the finer fringe element. This is due to the ill conditioned mass matrix issues discussed in Section 2.3 and shown in Figure 4. Therefore, while it does not effect the solution significantly, it is best practice to remove as little of the overlap from the finer fringe element as possible for the sake of maintaining numerical stability.

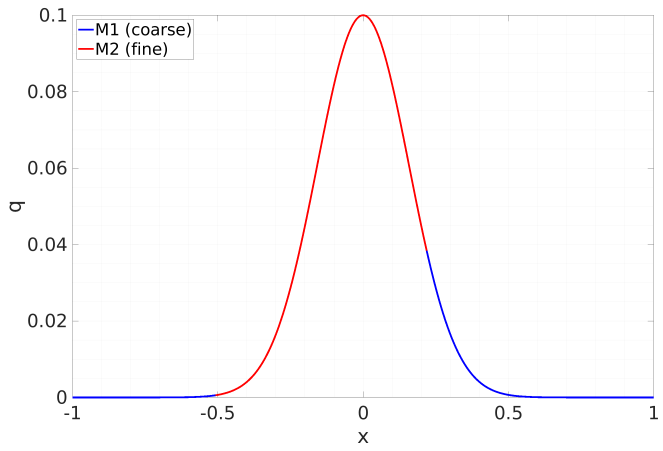

Figure 10: The initial condition for the 1D linear advection case. The colors indicate the regions corresponding to the two grids with blue being the coarse grid and red being the fine grid.

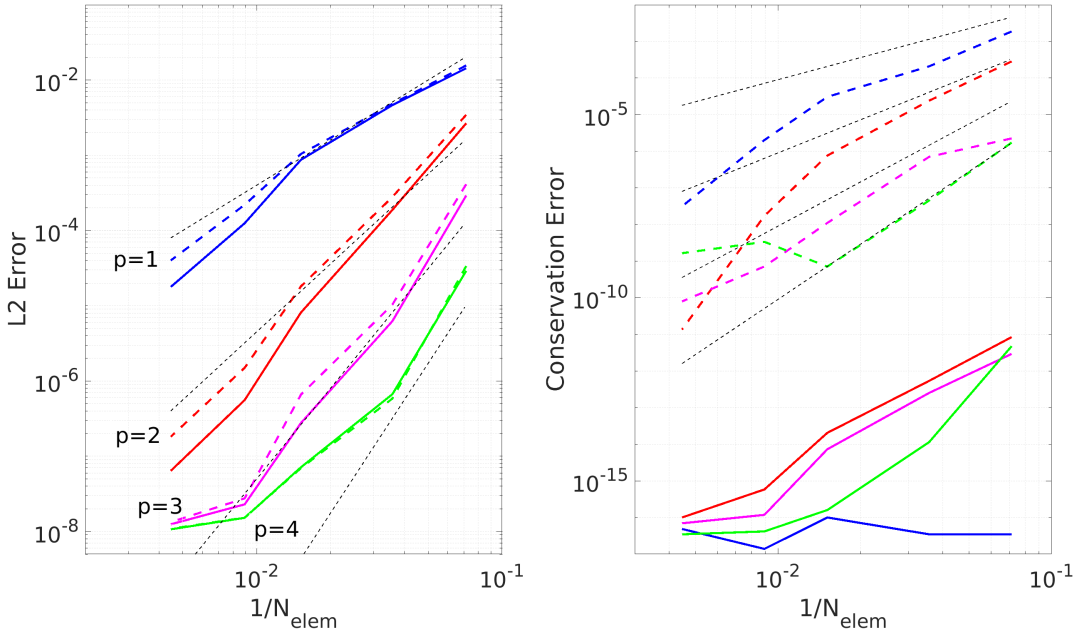

Figure 11: Convergence plots showing the L2 and conservation error for the baseline overset (dashed lines) and conservative overset (solid lines) from p=1 to 4. (—): p = 1, (—): p = 2, (—): p = 3, (—): p = 4, (- - -): ideal reference line

Table 1: Effect of cut proportion on the L2 error for the p=1 linear advection cases using conservative overset

% Overlap Cut from M1	% Overlap Cut from M2	$dx_1 = 0.25$, $dx_2 = 0.125$	$dx_1 = 0.125$, $dx_2 = 0.0625$	$dx_1 = 0.0625$, $dx_2 = 0.03125$	$dx_1 = 0.03125$, $dx_2 =$ 1.5625e-2
100	0	1.4330e-02	4.6395e-03	8.7225e-04	1.2487e-04
50	50	1.4483e-02	4.7308e-03	8.8611e-04	1.2613e-04
0	100	1.5377e-02	4.9453e-03	9.1376e-04	1.2823e-04

Table 2: Effect of cut proportion on the conservation error for the p=1 linear advection cases using conservative overset

% Overlap Cut from M1	% Overlap Cut from M2	$dx_1 = 0.25$, $dx_2 = 0.125$	$dx_1 = 0.125$, $dx_2 = 0.0625$	$dx_1 = 0.0625$, $dx_2 = 0.03125$	$dx_1 = 0.03125$, $dx_2 =$ 1.5625e-2
100	0	3.4694e-17	3.4694e-17	0.0000e+00	1.3878e-17
50	50	6.9389e-18	2.0817e-17	6.9389e-18	6.9389e-18
0	100	4.1633e-17	2.7756e-17	6.9389e-18	7.6328e-17

3.2 1D Inviscid Burger's Equation

In order to understand the conservative overset method's ability to handle nonlinear problems involving shocks, the inviscid Burger's equation (Eq. (20)) is modeled.

$$u_{,t} + \frac{1}{2}(u^2)_{,x} = 0 \tag{20}$$

The same problem of the advecting hill (see Figure 10 and Equation (17)) was studied. For Burger's equation, no exact solution is known so instead only the conservation error of the solution at t = 2 is shown. Once again, the timestep size is chosen such that it corresponds to a constant CFL = 0.05 based on the finest grid spacing.

As the hill advects forward, the regions of higher u advect more quickly than the rest of the domain due to the nonlinear nature of the problem. This causes a shock to form which then will pass through the overset boundary. In order to smoothly capture this shock and maintain numerical stability, the generalized Π^N slope limiter with the modified minmod function [12, 13, 14] is implemented for this problem.

The flowfield is presented for various mesh refinement and orders of accuracy in Figure 12. On the coarsest grids (shown in the top row), there are some observable differences between the baseline and conservative overset solutions at the fringe elements however overall the differences remain small. Oscillations are observed to appear before and after the shock location at $x \approx 0.4$, especially on coarser meshes. The amplitude of these oscillations decreases as the mesh is either refined or the order of accuracy is increased. On the finest grid using linear elements, the oscillations have been greatly diminished.

Comparisons of the conservation error for the cases shown in Figure 12 are shown in Tables 3 to 5. The conservation error of the single mesh case is added for reference. Since there is no oversetting in the single mesh case, the conservation error remains low. As was observed in the linear advection case, the baseline overset method introduces noticeable error due to the doubly counted overlap region and the differences in fluxes exchanged between meshes, whereas the conservative overset method is similar to the single mesh case. Interestingly, the errors do not decrease as the order of accuracy is increased for either overset method. Furthermore, the errors do not decrease dramatically as the mesh is refined. The reason for this appears to be the slope limiter forcing the solution down to linear orders of accuracy near the shock. The error caused by the slope limiter in this p=1 region is enough to mask the improvements caused by using higher order bases.

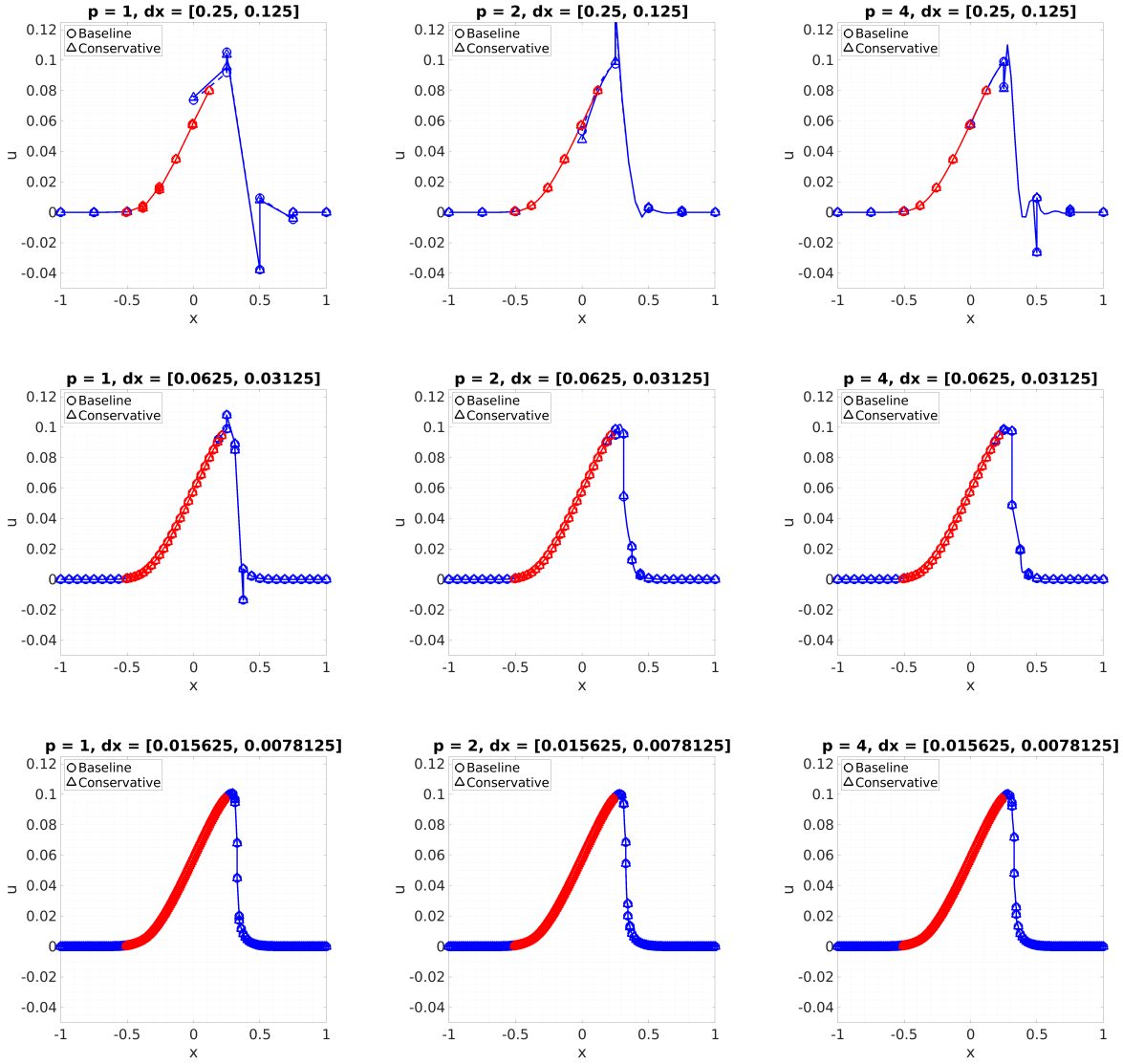

Figure 12: Comparison of the solution from the baseline overset (O) and the conservative overset (Δ) methods for various mesh resolution and orders of accuracy at t = 2 for the inviscid Burger's equation. The blue curves indicate the coarse mesh solution while the red indicates the finer mesh solution.

Table 3: Conservation error for the inviscid Burger's equation cases with dx = [0.25,0.125]

	p = 1	p = 2	p = 3	p = 4
Single Mesh	3.4694e-17	2.7756e-17	5.5511e-17	2.0817e-17
Baseline Overset	1.6698e-03	2.6566e-03	2.6114e-03	2.6113e-03
Conservative Overset	4.1633e-17	1.4085e-12	1.1091e-11	1.7699e-11

Table 4: Conservation error for the inviscid Burger's equation cases with dx = [0.0625, 0.03125]

	p = 1	p = 2	p = 3	p = 4
Single Mesh	2.0817e-17	1.3270e-11	1.6389e-11	9.1699e-11
Baseline Overset	1.1935e-03	1.1583e-03	1.1576e-03	1.1577e-03
Conservative Overset	1.3184e-16	1.3034e-11	1.6043e-11	1.3837e-10

Table 5: Conservation error for the inviscid Burger's equation cases with dx = [0.015625, 0.0078125]

	p = 1	p = 2	p = 3	p = 4
Single Mesh	6.8001e-16	1.3861e-11	2.0708e-11	9.0906e-10
Baseline Overset	4.8087e-05	4.9849e-05	4.9865e-05	4.9864e-05
Conservative Overset	1.5266e-16	1.3743e-11	2.0316e-11	9.1472e-10

3.3 2D Euler

The 2D Euler equations are shown below.

$$\begin{aligned} \rho_{,t} + (\rho u)_{,x} + (\rho v)_{,y} &= 0 \\ (\rho u)_{,t} + (\rho u u + p)_{,x} + (\rho u v)_{,y} &= 0 \\ (\rho v)_{,t} + (\rho u v)_{,x} + (\rho v v + p)_{,y} &= 0 \\ E_{,t} + (u(E+p))_{,x} + (v(E+p))_{,y} &= 0 \end{aligned} \tag{21}$$

where ρ is the fluid density, u is the x-velocity, v is the y-velocity, p is the pressure, E is the total energy, and t is time.

The problem of interest is an isentropic vortex advecting through two square overset grids, as shown in Figure 13. The two grids are composed of triangular elements and are oriented such that they overlap each other on only one end of the mesh. This configuration was chosen to allow the cut boundary to be a straight vertical line through the overlap region. As mentioned before in Section 2.4, when the conservative overset method is extended to two dimensions, finding the cut boundary between multiple grids is nontrivial. This configuration was also motivated by numerical stability. As with the 1D linear advection and Burger's equation simulations, issues with the ill-conditioned mass matrices of cut elements were encountered. Using the configuration shown in Figure 13 allowed for control of the overlap size and thus the amount by which each element was cut.

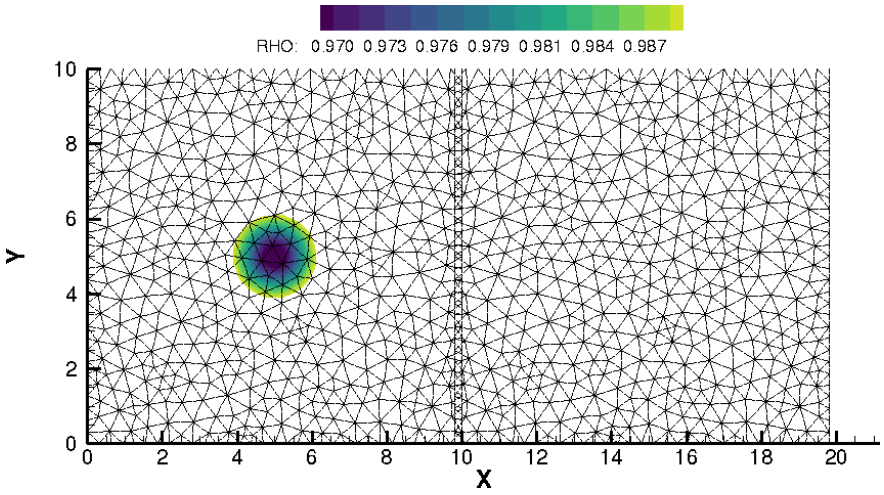

Figure 13: Initial condition and example grid configuration for the 2D Euler advecting vortex

The initial condition of the isentropic vortex is shown in Equations (22) and (23). As the vortex advects through the two domains, it should remain coherent and not experience any dissipation due to the nature of the Euler equations.

$$\begin{aligned} \rho(x,y) &= \frac{P(x,y)}{T(x,y)} \\ u(x,y) &= u_\infty - \Gamma(y-y_0)^2 \exp(0.5(1-r^2)) \\ v(x,y) &= v_\infty + \Gamma(x-x_0)^2 \exp(0.5(1-r^2)) \\ E(x,y) &= \frac{P(x,y)}{\gamma - 1} + \frac{1}{2}\rho(x,y)\left(u^2(x,y) + v^2(x,y)\right) \end{aligned} \tag{22}$$

given that

$$\begin{aligned} \Gamma &= \frac{1}{2\pi} \\ T(x,y) &= \frac{P_\infty}{\rho_\infty} - \frac{\Gamma^2}{2}\left(\frac{\gamma-1}{\gamma}\right)\exp(1-r^2) \\ P(x,y) &= \left(\frac{\rho_\infty^\gamma}{P_\infty}T(x,y)^\gamma\right)^{\frac{1}{\gamma-1}} \end{aligned} \tag{23}$$

where (x_0, y_0) is the coordinate of the vortex starting location, γ is the specific heat ratio, and the subscript $(\cdot)_\infty$ denotes freestream values. For the cases shown here, the following freestream values are used: $\{\rho_\infty, u_\infty, v_\infty, P_\infty\} = \{1.0,\ 0.2,\ 0.0,\ 0.714286\}$.

Characteristic boundary conditions are used on all of the outer boundaries of both grids. Time integration is performed using a 3 stage Runge-kutta method with a non-dimensional $\Delta t = 0.01$. The simulation is performed for 4000 time steps and the vortex convects 8 units in this time from its staring location at (5,5) on the first mesh to its final location at (13,5) on the second grid.

Images of the advecting vortex are shown at several instances in Figure 14 to demonstrate the qualitative ability of the 2D conservative overset to retain the coherency of the vortex as it passes through the cut overset interface. Error convergence studies are conducted using structured triangular grids that provide ease of refinement. The exact solution to the isentropic vortex at any given time is given by Equations (22) and (23) using a value of x_0 given by $x_0(t) = x_0(t) + u_\infty t$. L2 error is computed as the norm of difference between all the computed fields ($[\rho, \rho u, \rho v, E]$) and the corresponding exact solution. Since the outer boundary conditions are non-periodic, conservation errors have to be computed accounting for the fluxes at all of the outer boundaries. For example, at any time t, the mass conservation error can be computed as:

$$error_{cons}(t) = \left| \sum_{i=1}^{n_{elem}} \int_{\Omega_e} (\rho(x,y,0) - \rho(x,y,t))\, d\Omega_e - \int_0^t \left(\sum_{i=1}^{n_{of}} \int_{\Gamma_e^i} \hat{F}(x,y,\tau)_i \cdot \mathbf{n} d\Gamma_e^i \right) d\tau \right| \tag{24}$$

where Γ_e^i represent just the faces which lie on the outer boundary of the domain, n_{of} is the number of outer faces, and $\hat{F}(\tau)$ is the mass flux on an outer boundary faces at time τ. For the cut elements and cut faces, the integrals in the above equation have to be modified by subtracting the appropriate volume and boundary portions exactly in the same way as the volume and boundary discretization terms were constructed for cut elements.

The error convergence and corresponding time history of the L2 error for all primary field variables is shown in Figures 15 and 16, respectively. In both plots, comparisons are made between results for a dual-mesh conservative overset simulation and a single mesh simulation with identical domain size and element size are presented. Overall the conservative overset simulations show slightly higher L2 error compared to the single mesh simulation though it remains at the same order of magnitude. As expected, increasing order of accuracy reduces the error considerably and both methods show the expected error convergence rates as a function of Δx, i.e. $O(\Delta x^2)$ and $O(\Delta x^3)$ for p=1 and p=2 respectively. A time history of the conservation errors for the 4000 time steps simulated is shown in Figure 17 for both p=1 and p=2. The conservation error shows encouraging trends and remains low for both the single mesh and conservative overset cases.

4 Conclusion and Future Work

The focus of this work was to develop an overset methodology which preserved the conservation of the primary variables as fluid crossed the intermesh boundary. It was found that traditional methods incurred conservation error because of 1) the double computation of the overlap region by both grids and 2) the mismatch between the the fluxes entering and exiting each grid. To combat this, the formulation for the fringe elements was modified such that the overlap region was cleanly divided between each of the grids. This is conceptually similar to solving the equations on a single fully connected mesh, although no remeshing was required. Methods for implementing this cutting approach were discussed for both 1D and 2D grids.

The conservative overset method was first demonstrated on 1D linear advection and showed that it led to

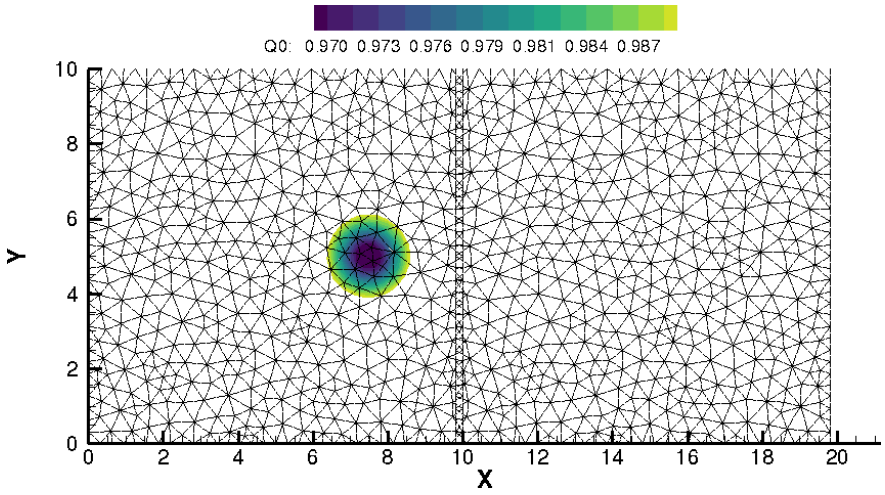

(a) t = 12.4 sec

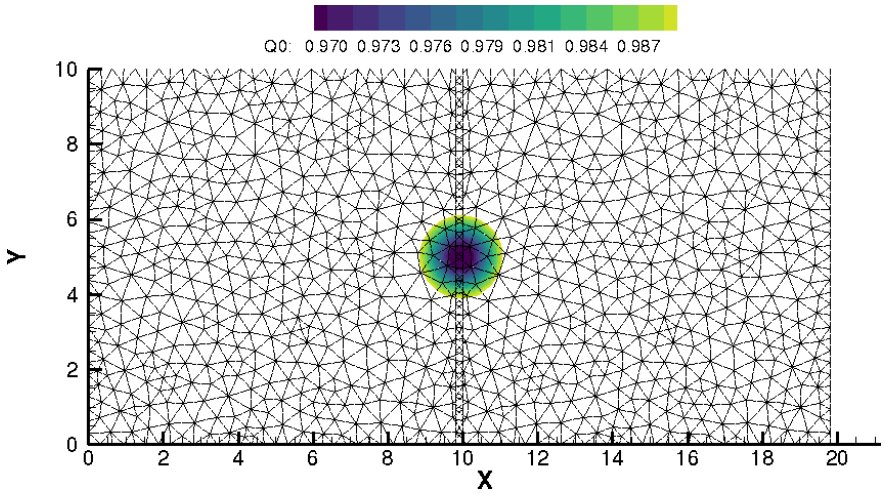

(b) t = 24.8 sec

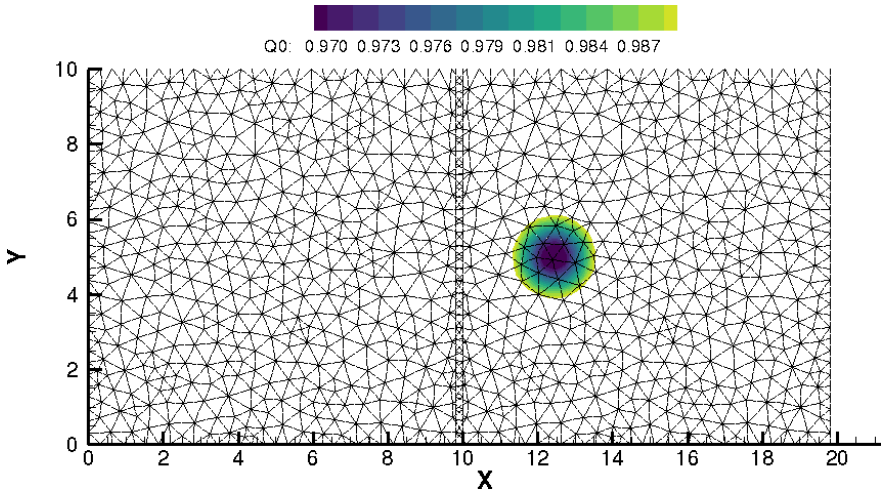

(c) t = 37.2 sec

Figure 14: Snapshots of the isentropic vortex advecting through the 2D domain using the conservative overset method.

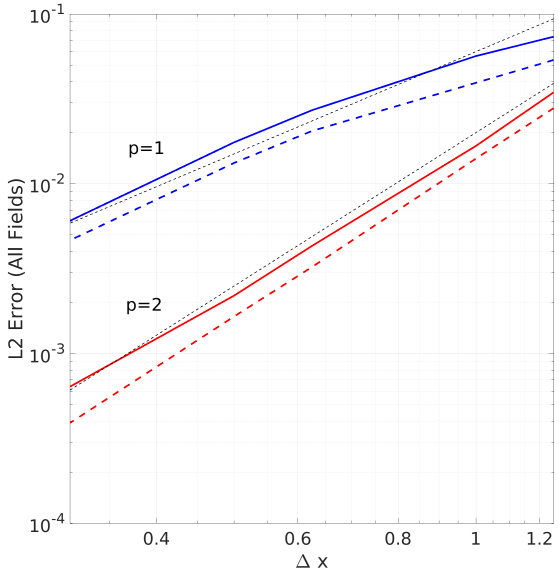

Figure 15: Convergence of the L2 error for the 2D Euler advecting vortex. (—): conservative overset p = 1, (- - -): single mesh p = 1, (—): conservative overset p = 2, (- - -): single mesh p = 2, (- - -): ideal reference line

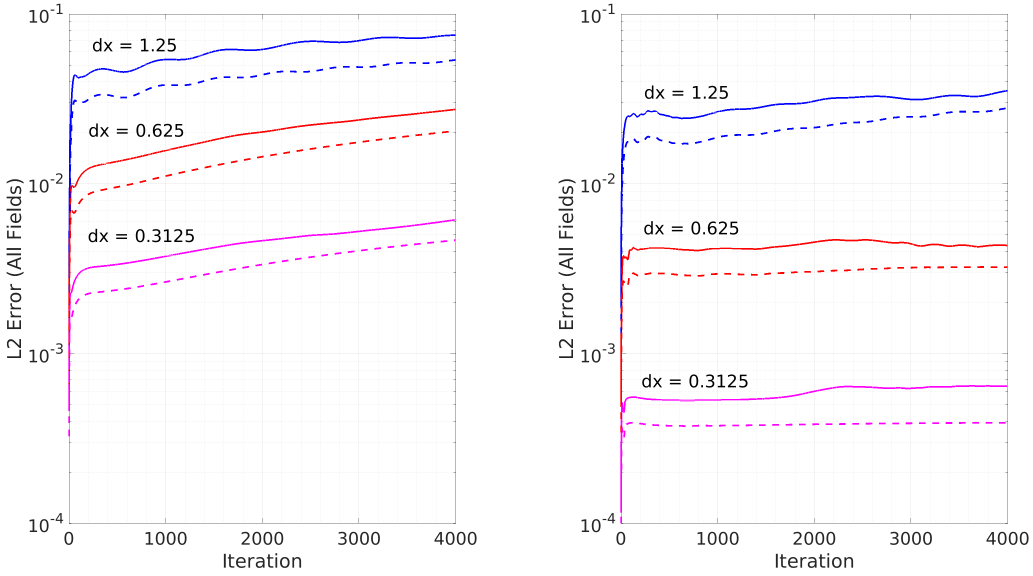

(a) p = 1

(b) p = 2

Figure 16: Time series of the L2 error for the 2D Euler advecting vortex flow at (a) p = 1 and (b) p = 2. (—): conservative overset, (- - -): single mesh

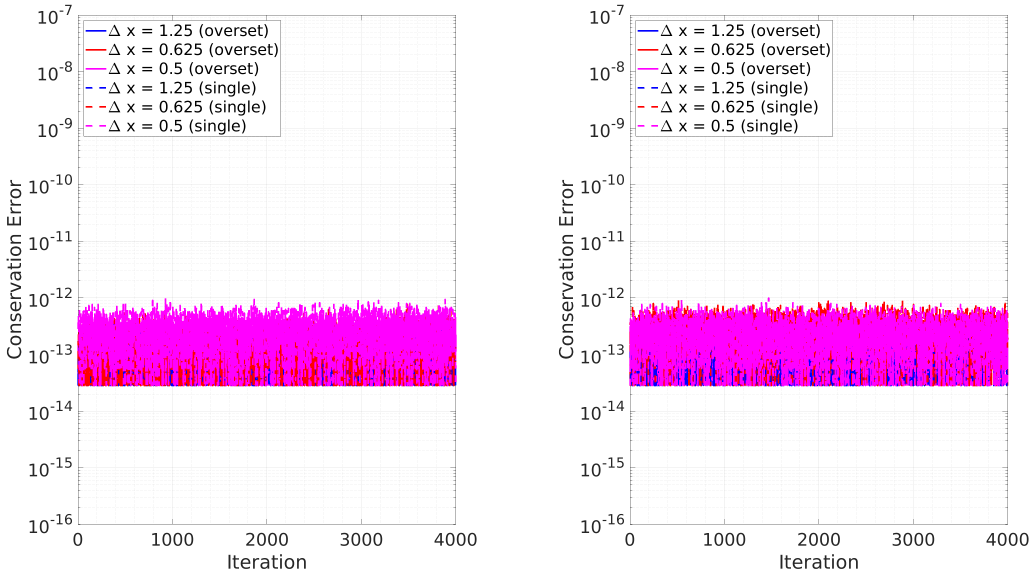

(a) p = 1 (b) p = 2

Figure 17: Time series of the conservation error for the 2D Euler advecting vortex at (a) p = 1 and (b) p = 2

a slight improvement in the convergence rate over the baseline overset. Its largest benefit was a significant reduction in the conservation error. Compared to the baseline overset method, the conservative method led to a 5-6 orders of magnitude reduction in conservation error. For finer grids, the conservation error was reaching machine zero. Similar results were shown when extending this method to nonlinear problems involving shockwaves for the inviscid Burger's equation. The conservative overset method demonstrated conservation errors at the same level as the single mesh case while the baseline overset case showed significantly higher errors. The conservative method was also extended to a 2D advecting vortex using the Euler equations and it was shown once again that the L2 and conservation errors were on par with that of the single mesh case.

Overall this method was found to be effective however its primary drawbacks are its numerical stability and the ability to find appropriate cut boundaries for 2D and 3D grids. These two aspects are related as the numerical stability of the method depends on the proportion of the element being cut. Severely cutting fringe elements creates ill-conditioned mass matrices which in turn often lead to divergent solutions. This effect can be minimized through careful choice of a cut boundary which minimizes the amount of each element being cut, though this may be difficult to do in general. Numerical tools may also be implemented to improve stability. For instance, in this work L2 regularization was used during the mass matrix inversion. This technique was found to be effective at increasing stability though was not sufficient for all cases. In the future, methods for finding optimal cut boundaries as well as alternative numerical methods for improving stability will be explored.

This work is still in its early stages and there remains much research to be done on the topic. Of particular interest are improving the stability of the method, developing of efficient cutting algorithms for 2D cases, developing methods for cutting larger numbers of meshes, introducing viscous fluxes, and ultimately implementing the conservative overset method for 3D unstructured moving grids.

References

[1] Kai-Hsiung Kao and Meng-Sing Liou. Advance in overset grid schemes-from chimera to DRAGON grids. *AIAA journal*, 33(10):1809–1815, 1995.

[2] Nathan Hariharan, Z Wang, Pieter Buning, Nathan Hariharan, Z Wang, and Pieter Buning. Application

of conservative chimera methodology in finite difference settings. In *35th Aerospace Sciences Meeting and Exhibit*, page 627, 1997.

[3] Mun Seung Jung and Oh Joon Kwon. A conservative overset mesh scheme via intergrid boundary reconnection on unstructured meshes. In *19th AIAA Computational Fluid Dynamics*, page 3536. 2009.

[4] Philip Cali and Vincent Couaillier. Conservative interfacing for overset grids. In *38th Aerospace Sciences Meeting and Exhibit*, page 1008, 2000.

[5] Sâm A Landier, Stephanie Peron, and Thomas Renaud. New CFD capabilities based on intersecting arbitrary polyhedral meshes: P1-conservative interpolations and overset cfd applications. In *2018 AIAA Aerospace Sciences Meeting*, page 1498, 2018.

[6] Dominic DJ Chandar. On overset interpolation strategies and conservation on unstructured grids in openfoam. *Computer Physics Communications*, 239:72–83, 2019.

[7] David A Kopriva, Jan Nordström, and Gregor J Gassner. On the theoretical foundation of overset grid methods for hyperbolic problems: Well-posedness and conservation. *Journal of Computational Physics*, 448:110732, 2022.

[8] Marshall Galbraith, Paul Orkwis, and John Benek. Extending the discontinuous Galerkin scheme to the chimera overset method. In *20th AIAA Computational Fluid Dynamics Conference*, page 3409, 2011.

[9] Jacob Crabill, Freddie D Witherden, and Antony Jameson. A parallel direct cut algorithm for high-order overset methods with application to a spinning golf ball. *Journal of Computational Physics*, 374:692–723, 2018.

[10] Zhaowen Duan and Zhi J Wang. A high order overset FR/CPR method for dynamic moving grids. In *AIAA Scitech 2019 Forum*, page 1399, 2019.

[11] Veer N Vatsa, James L Thomas, and Bruce W Wedan. Navier-Stokes computations of a prolate spheroid at angle of attack. *Journal of Aircraft*, 26(11):986–993, 1989.

[12] Chi-Wang Shu. TVB uniformly high-order schemes for conservation laws. *Mathematics of Computation*, 49(179):105–121, 1987.

[13] Bernardo Cockburn. Discontinuous Galerkin methods for convection-dominated problems. In *High-order methods for computational physics*, pages 69–224. Springer, 1999.

[14] Jan S Hesthaven and Tim Warburton. *Nodal discontinuous Galerkin methods: algorithms, analysis, and applications*. Springer Science & Business Media, 2007.